Multi-scale Simulation for the Columnar to Equiaxed Transition in the Weld Pool

Rihong HAN, Shanping LU,* Wenchao DONG, Dianzhong LI and Yiyi LI

Shenyang National Laboratory for Materials Science, Institute of Metal Research, Chinese Academy of Sciences, 72 Wenhua Road, Shenyang, 110016 China.

The heat and mass transfer behavior and the morphological evolution of the solidification structures in the weld pool were simulated by the multi-scale model which combines the finite element (FE) and the cellular automata (CA) methods to investigate the columnar to equiaxed transition (CET) process during welding. The grain structure evolution within the entire weld and the competitive dendrite growth at different locations were studied to better understand the CET process. The results indicate that with the decrease of the distance to weld center, the undercooled zone width and the maximum undercooling increase. In this case, more equiaxed dendrites form in the undercooled melt, and the distance between the equiaxed dendrites and the columnar front also becomes lager. There is more space for the equiaxed dendrites to grow up and block the columnar dendrites. Therefore, the equiaxed dendrites become more competitive, and the CET tendency increases.

KEY WORDS: numerical simulation; weld solidification; competitive dendrite growth; cellular automata.

1. Introduction

Fusion welding has a wide range of applications in the manufacturing industry field.[1] The morphology of the solidification structure in the molten pool controls the ultimate mechanical properties of the weld.[2] The columnar to equiaxed transition (CET) in the weld produce the continuous equiaxed grain zone in the weld as shown in **Fig. 1**,[3] which can obviously refine the grain and improve the mechanical properties of the weld. Therefore, in order to obtain the finer equiaxed grain structure and the better mechanical properties of the weld, the study on the CET phenomenon during welding should be performed to provide the useful information for the welding parameter optimization. The various grain structure morphologies in the weld is directly determined by the competitive growth of microstructures with different preferential orientations in the molten pool. The welding parameters exert an important influence on the grain structure evolution through changing the solidification conditions. As a result, to better understand the CET process during welding, it is necessary to investigate the competitive growth of microstructures in the molten pool. However, owing to the complicated welding process, it is difficult to observe the highly dynamic solidification behavior.

With the development of the numerical technique, the solidification structure morphology in the molten pool could be simulated directly by the Phase field (PF) and the cellular automata (CA) methods. Pavlyk[4] simulated the dendrite morphology in the molten pool of gas tungsten arc welding (GTAW) by the CA model. Y. Wei[5] developed a numerical model based on CA technique to study the columnar dendritic grain growth at the edge of the weld pool. X. Zhan[6,7] proposed a limited angles method to improve the CA model and simulated the competitive dendrite growth in the molten pool. R. Ma[8] and Z. Dong[9] investigated the dendrite morphology and the solute redistribution with the fluid flowing in the weld pool. The dendrite growth in the laser-engineered net shaping process was studied by Yin[10] using a two-dimensional model combining the FE and CA methods. The grain structure morphology in the weld of GTAW was simulated by Chen[11] and Bordreuil[12] using the CA model. Tan and Shin[13–15] proposed a two-dimensional CA-PF model to study the dendrite and grain growth in the
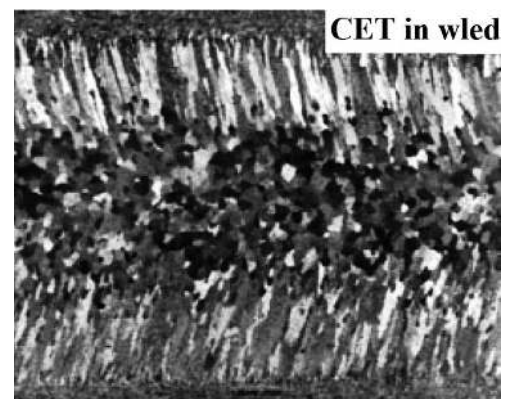

Fig. 1. The equiaxed grain structure in the gas tungsten arc (GTA) weld.[3] The welds shown in this figure are full penetrated in order to obtain the two-dimensional solidification structures.

molten pool. Farzadi[16] and Fallah[17] simulated the dendrite morphology evolution in the molten pool using the PF method. The microstructure evolution with the transient solidification conditions was simulated by W. Zheng[18,19] using the PF model. A review of these studies shows that the dendrite morphology evolution was investigated, and the grain structure in the weld was also simulated through coupling the macro-scale heat transfer model. As mentioned above, the CET process during welding is directly controlled by the competitive growth of the microstructures under the transient thermal conditions within the entire molten pool. Therefore, to comprehensively understand the CET process, both the transient solidification conditions along the trailing pool boundary and the competitive growth of the solidification structures should be considered. However, the multi-scale study for the CET process during GTAW which contains the heat and mass transfer in the molten pool, the grain structure evolution within the entire weld, and the competitive growth of microstructures has not been presented.

In the present work, the FE model and the CA technique are adopted to simulate the heat and mass transfer behavior and the morphological evolution of the solidification structures in the weld, respectively. The solidification conditions along the trailing pool boundary have been extracted and analyzed. The morphological evolution of the grain structure within the entire weld is simulated to show the complete CET process during welding. The calculation conditions used in the CA model are obtained from the results of the FE model through the interpolation method. In addition, the simulation for the competitive growth of microstructures at different locations is also performed to further understand the CET process at micro-scale.

2. The Model Description

The heat and mass transfer behavior during welding is calculated by a three-dimensional FE model to obtain the transient solidification conditions in the weld pool. In this model, the complicated fluid flow in the molten pool is considered. To simplify the numerical model, some basic assumptions have been made as follows: (1) this problem is symmetric in the longitude plane along the welding direction, (2) the fluid flow in the welding pool is laminar, incompressible and Newtonian, and (3) the deformation of the free surface during welding process is ignored. To calculate the heat and mass transfer process, it is necessary to solve the equations of energy, mass and momentum conservation. These conservation equations in three-dimensional Cartesian coordinate system are shown as follows.[20]

$$\frac{\partial(\rho u)}{\partial x} + \frac{\partial(\rho v)}{\partial y} + \frac{\partial(\rho w)}{\partial z} = 0 \quad \cdots\cdots\cdots\cdots (1)$$

$$\rho\left[\frac{\partial u}{\partial t} + u\frac{\partial u}{\partial x} + v\frac{\partial u}{\partial y} + w\frac{\partial u}{\partial z}\right]$$
$$= -\frac{\partial p}{\partial x} + \frac{\partial}{\partial x}\left(\mu\frac{\partial u}{\partial x}\right) + \frac{\partial}{\partial y}\left(\mu\frac{\partial u}{\partial y}\right) + \frac{\partial}{\partial z}\left(\mu\frac{\partial u}{\partial z}\right) + S_x \quad \cdots (2)$$

$$\rho\left[\frac{\partial v}{\partial t} + u\frac{\partial v}{\partial x} + v\frac{\partial v}{\partial y} + w\frac{\partial v}{\partial z}\right]$$
$$= -\frac{\partial p}{\partial y} + \frac{\partial}{\partial x}\left(\mu\frac{\partial v}{\partial x}\right) + \frac{\partial}{\partial y}\left(\mu\frac{\partial v}{\partial y}\right) + \frac{\partial}{\partial z}\left(\mu\frac{\partial v}{\partial z}\right) + S_y \quad \cdots (3)$$

$$\rho\left[\frac{\partial w}{\partial t} + u\frac{\partial w}{\partial x} + v\frac{\partial w}{\partial y} + w\frac{\partial w}{\partial z}\right]$$
$$= -\frac{\partial p}{\partial z} + \frac{\partial}{\partial x}\left(\mu\frac{\partial w}{\partial x}\right) + \frac{\partial}{\partial y}\left(\mu\frac{\partial w}{\partial y}\right) + \frac{\partial}{\partial z}\left(\mu\frac{\partial w}{\partial z}\right) + S_z \quad \cdots (4)$$

$$\rho C_p\left[\frac{\partial T}{\partial t} + u\frac{\partial T}{\partial x} + v\frac{\partial T}{\partial y} + w\frac{\partial T}{\partial z}\right]$$
$$= \frac{\partial}{\partial x}\left(K\frac{\partial T}{\partial x}\right) + \frac{\partial}{\partial y}\left(K\frac{\partial T}{\partial y}\right) + \frac{\partial}{\partial z}\left(K\frac{\partial T}{\partial z}\right) + S_H \quad \cdots\cdots (5)$$

where ρ is the density of the metal, u, v, w are velocities of the liquid metal, S_x, S_y, S_z are the volume forces in the molten pool, K is the thermal conductivity, C_p is the specific heat, S_H is the latent heat. The solidification structure evolution in the weld pool occurs in the three-dimensional space. However, the solidification conditions and the grain structure in the weld can be simplified if the thin plate-shaped workpiece and the full penetration process are applied. In this case, the solidification conditions and the grain structure in the weld do not change obviously along the thickness direction of the workpiece and can be approximately considered as two-dimensional problems. As a result, the workpiece used in the FE model is a carbon steel plate with the length of 100 mm, width of 50 mm, and thickness of 2 mm. This method also adopted by many previously reported experimental investigations for the grain structure evolution in the weld.[21–24] To obtain the full penetrated weld, the welding current is 110 A, the voltage is 12 V, and the speed is 1.5 mm/s in the simulation. The material properties of the carbon steel are obtained from the reference.[25] The CA technique is adopted to simulate the solidification structure morphology in the molten pool. The physical properties of the Fe–C binary alloy used in the calculation are listed in **Table 1**.[26,27] The solute distribution in the molten pool is solved by the equation as follows:[28]

$$\frac{\partial C_i}{\partial t} = D_i \cdot \nabla^2 C_i + C_i \cdot (1-k)\frac{\partial f_s}{\partial t} \quad \cdots\cdots\cdots\cdots (6)$$

Table 1. Physical properties of the Fe–C alloy.[26,27]

Physical property	Value
Density, ρ (kg/m^3)	7 200
Latent heat, L (J/kg)	2.47×10^{-5}
Liquidus temperature, T_L (K)	1 763
Liquidus slope, m_l (K/wt.%)	−80
Equilibrium partition coefficient, k	0.34
Gibbs-Thomson coefficient, Γ (K m)	1.9×10^{-7}
Solute diffusion coefficient in the liquid, D_L (m^2/s)	2×10^{-9}
Solute diffusion coefficient in the solid, D_S (m^2/s)	5×10^{-10}
Alloy initial composition, C_0 (wt.%)	0.6

where C is the solute concentration, D is the solute diffusivity, the subscript i indicates liquid or solid, and f_s is the solid fraction. The local curvature of the S/L interface is calculated by[26]

$$K = \left[\left(\frac{\partial f_s}{\partial x} \right)^2 + \left(\frac{\partial f_s}{\partial y} \right)^2 \right]^{-3/2}$$
$$\times \left[2 \frac{\partial f_s}{\partial x} \frac{\partial f_s}{\partial y} \frac{\partial^2 f_s}{\partial x \partial y} - \left(\frac{\partial f_s}{\partial x} \right)^2 \frac{\partial^2 f_s}{\partial y^2} - \left(\frac{\partial f_s}{\partial y} \right)^2 \frac{\partial^2 f_s}{\partial x^2} \right] \quad \text{... (7)}$$

According to the results of the actual temperature and the local interface curvature, the interface equilibrium composition C_l^* can be obtained by[26]

$$C_l^* = C_0 + \frac{T^* - T^{eq}}{m_l} + \frac{\Gamma K f(\varphi, \theta)}{m_l} \quad \text{................ (8)}$$

where C_0 is the initial composition, T^* is the actual temperature calculated by the FE model, T^{eq} is the liquidus at the initial solute composition, m_l is the liquidus slope, and Γ is the Gibbs-Thomson coefficient. The $f(\varphi, \theta)$ is the surface tension anisotropy function and can be calculated by[26]

$$f(\varphi, \theta) = 1 - \delta \cos\left[4(\varphi - \theta) \right] \quad \text{.................. (9)}$$

where φ is the angle between the x-axis and the normal to S/L interface, θ is the preferential orientation of the nucleus, and δ is the anisotropic coefficient. According to the gradient of solid fraction at the S/L interface, φ can be calculated by:[26]

$$\varphi = \cos^{-1}\left[\frac{\partial f_s / \partial x}{((\partial f_s / \partial x)^2 + (\partial f_s / \partial y)^2)^{1/2}} \right] \quad \text{......... (10)}$$

The growth velocity of the solidification structure is controlled by the increase of solid fraction in the interface cells which can be obtained by[28]

$$\Delta f_s = (C_l^* - C_l) / (C_l^* \cdot (1 - k)) \quad \text{................ (11)}$$

In the calculation, a random fluctuation F_{fs} has been added to the solid fraction increment for the interface cells to simulate the sidebranch formation, which can be calculated by

$$F_{fs} = A_{fs} \cdot R_{fs} \quad \text{............................. (12)}$$

where A_{fs} is the coefficient, and R_{fs} is the random number in the range of $[-1, 1]$. The description of the capturing algorithm for the new interface cells is shown in reference.[29] The nucleation of equiaxed grains is important for the CET in the weld and determined as a function of the undercooling. A continuous Gaussian nucleation distribution is adopted to relate the nuclear density increase to the increased effective undercooling. The total number of the nuclei for a given ΔT can be obtained by:[30–32]

$$n(\Delta T) = \frac{N_{max}}{\sqrt{2} \Delta T_\sigma} \int_0^{\Delta T} \exp\left[-\frac{(\Delta T - \Delta T_N)^2}{2(\Delta T_\sigma)^2} \right] d(\Delta T) \quad \text{... (13)}$$

where ΔT_N is the mean nucleation undercooling, ΔT_σ is the standard deviation of the distribution and N_{max} is the maximum nucleation density. The above nucleation parameters control the number and the location of the equiaxed grains in the weld during solidification. To obtain the complete

CET process in the weld under the welding parameters used in the simulation, the N_{max} is 1×10^{10} m^{-3}, the ΔT_N is 11 K, and the ΔT_σ is 1 K in the calculation. Since the FE mesh is much larger than the CA mesh, the bilinear interpolation method is adopted which is described in reference.[10]

3. Results and Discussions

3.1. Model Test

The tip velocity and the equilibrium composition of an equiaxed dendrite of the Fe-0.6 wt.% C alloy in the undercooled melt are calculated to verify the accuracy of the developed CA model. **Figure 2**(a) shows the variation of the tip velocity with the solidification time. At the beginning, the tip velocity is much larger than the steady value. With the increase of the solidification time, the tip velocity decreases owing to the solute accumulation in front of the S/L interface. The dendrite growth comes to the steady stage when
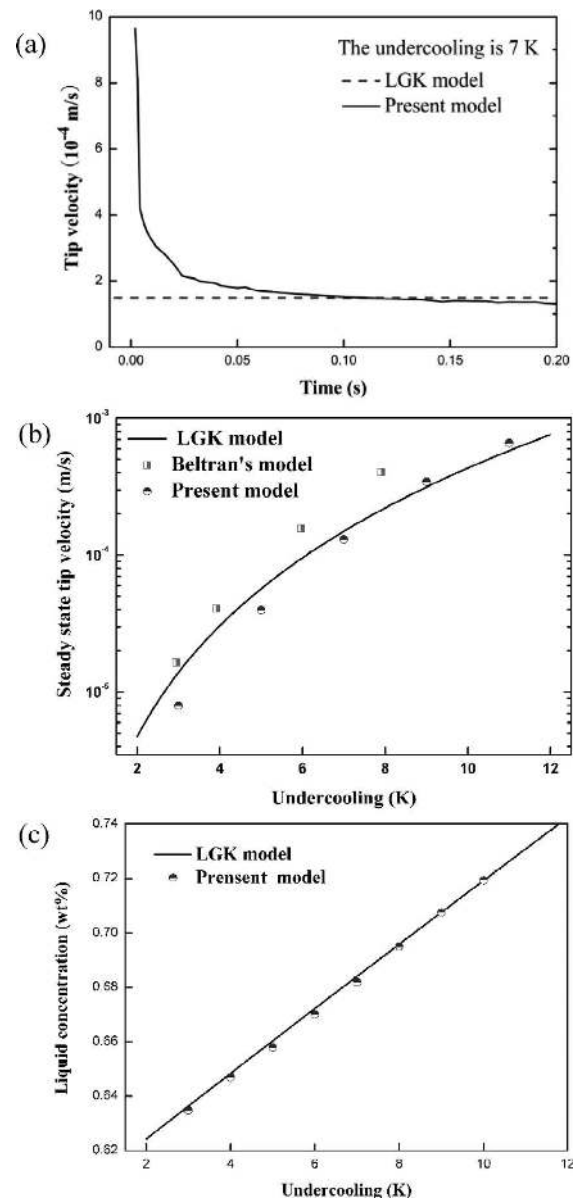

Fig. 2. (a) The variation of the tip velocity with the solidification time at 7 K undercooling. (b) The steady tip velocities calculated by the present CA model and other previous models[33,34] for different undercoolings. (c) The equilibrium compositions for different undercoolings.

the rejected solute is equal to that which can be transferred away.[28] Figure 2(b) shows the steady tip velocity for different undercoolings. It can be observed that the scaling of the tip velocity calculated by the present CA model is consistent with the results from the LGK analytical model[33] and the other published numerical model.[34] The actual solidification conditions in the weld pool is more complicated. In order to guarantee the rationality of the model, a constant low welding speed is adopted in the following calculation to obtain the steady welding process and the small solidification rate of the grains. The solute accumulated in front of the S/L interface during the crystal growth can affect the undercooling distribution in the liquid. Therefore, the equilibrium compositions for various undercoolings calculated by the present CA model are also compared with the results of the LGK model as shown in Fig. 2(c). It can be seen that the agreement of the equilibrium composition values appears to be good. The accurate simulation for the dendrites with random preferential orientations is important for the investigation of the competitive dendrite growth in the molten pool. **Figure 3** shows the simulated results of equiaxed dendrites with various preferential orientations. It can be observed that the actual growth direction of each dendrite agrees well with its defined direction.

3.2. Grain Structure Evolution in the Entire Weld

Figure 4 shows the simulated result of the temperature field on the upper surface of the workpiece. It can be observed that an elliptical-shaped molten pool forms during welding owing to the moving heat source. The CET process in the weld is controlled by the competitive growth between the columnar grains from the fusion line and the new equiaxed grains in the undercooled molten pool, which is affected directly by the transient solidification conditions. **Figure 5**(a) illustrates the temperature gradient G along the trailing pool boundary. It can be observed that with the

decrease of the distance to the weld center, the temperature gradient at the trailing pool boundary decreases from 568.3 to 185.4 K/mm. The solidification rate along the normal to trailing pool boundary is related with the weld pool shape and can be expressed as follows:[35]

$$R = V_{welding} \cdot \cos(\alpha) \quad \text{................} (14)$$

where R is the solidification rate, $V_{welding}$ is the welding speed, and α is the angle between the welding direction and the normal to trailing pool boundary. The angel α and the solidification rate along the trailing pool boundary are shown in Fig. 5(b). The cooling rate during solidification, which is equivalent to the product, $G \times R$, affects the micro-
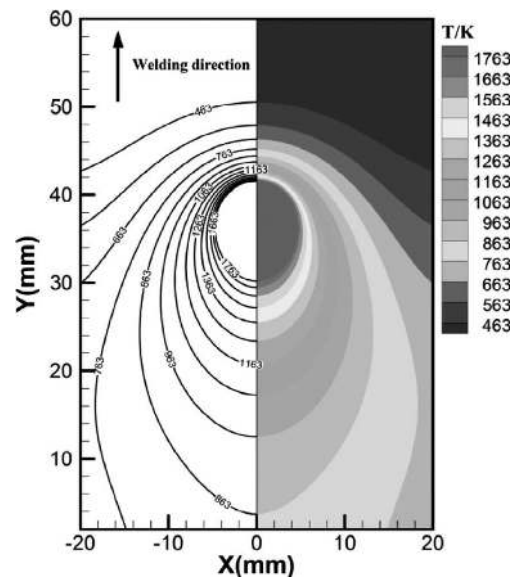

Fig. 4. Simulated results of temperature field on the upper surface of the workpiece. The welding speed is 2 mm/s, the welding current is 110 A, and the voltage is 12 V.
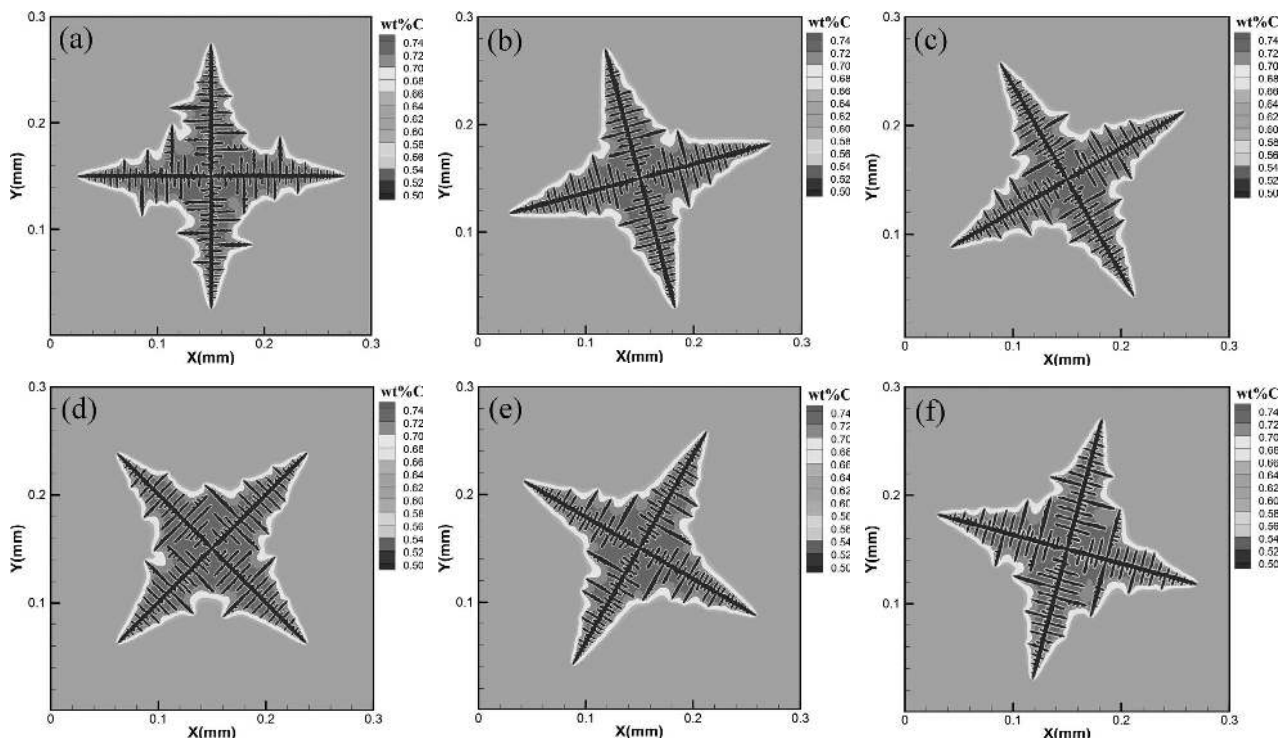

Fig. 3. The morphologies of equiaxed dendrites of the Fe-0.6 wt.% C alloy with the preferential orientations of (a) 0, (b) 15, (c) 30, (d) 45, (e) 60 and (f) 75 °, respectively.
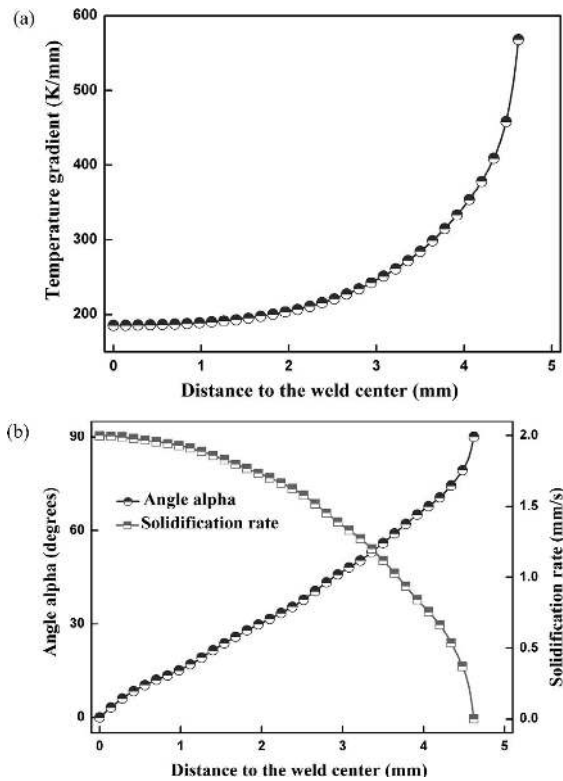
Fig. 5. The (a) temperature gradient, the (b) angle α and the solidification rate along the trailing pool boundary. The x axis is the distance to the weld center.

Fig. 6. The G×R and G/R along the trailing pool boundary. The x axis is the distance to the weld center.

Fig. 7. The simulated results for the morphological evolution of the grain structure within the entire weld.

structure scale in the weld. The ratio, G/R, largely determines the solidification structure morphology.[36)] **Figure 6** shows the cooling rate and the ratio, G/R, along the trailing pool boundary. It can be observed that with the decrease of the distance to the weld center, the cooling rate during solidification increases from 0 to 370.8 K/s, and G/R decreases from 258×10^7 to 9.27×10^7 K s m^{-2}.

Figure 7 illustrates the grain structure evolution in the entire molten pool during welding. The calculation domain is the left half of the weld. It can be seen that the solidification of weld pool begins from the epitaxial growth on the partially melted substrate grains located at the fusion line.[3)] Then the competitive growth of grains with random preferential orientations occurs during the solidification process. The grains with the preferential orientations closer to the highest temperature gradient direction will be more competitive and block those less favorably oriented grains. It is difficult to find the equiaxed grains near the fusion line. With the growth of the columnar grains toward the weld center, the highest temperature gradient direction moves closer to the welding direction. It is worth noticing that the columnar grains will not curve with the change of the highest temperature gradient direction owing to the anisotropic growth kinetics for the dendritic structure. With the development of solidification, a few equiaxed grains begin to form in the weld. However, compared with the columnar grains, these equiaxed grains are less competitive and surrounded by the columnar grains after solidification. With the decrease of the distance to the weld center, the equiaxed grains increase gradually and finally block the columnar grains from the fusion line. The above results indicate that the CET process is directly related with the competition between the columnar and equiaxed grains which is controlled by the solidification conditions.
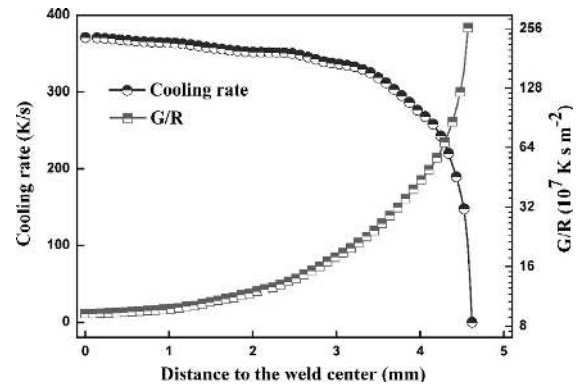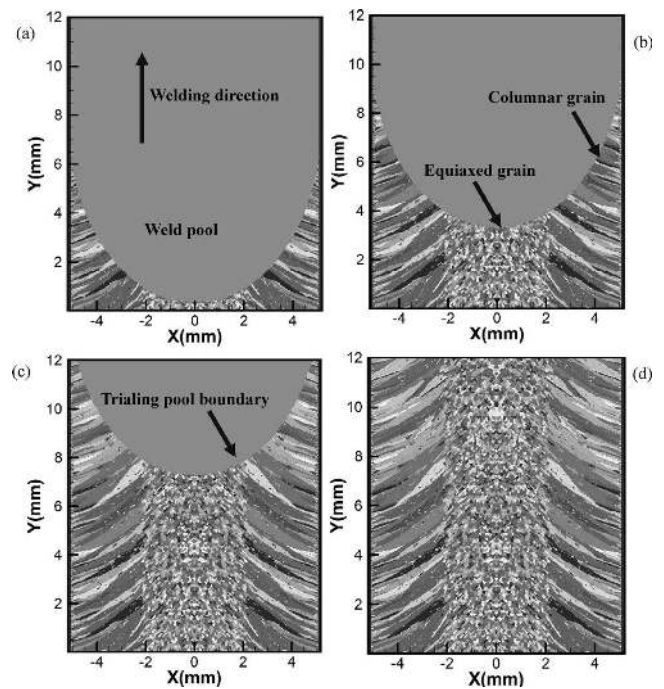
Owing to the limitation of the computational coefficient, the coarser mesh with the length of 4 μm is used in the calculation for the grain structure evolution shown in Fig. 7 to qualitatively illustrate the complete CET process in the entire weld. However, this result can not quantitatively reflect the morphological evolutions of the columnar and equiaxed dendrites which are important to understand the micro-mechanism for the CET. In order to obtain more detailed information and better understand the CET mechanism, the micro-scale simulation for the competitive dendrite growth under various solidification conditions should be performed.

3.3. Competitive Dendrite Growth During CET

The competitive dendrite growth at different locations along the trailing pool boundary has been simulated in this section. The calculation domain is 0.5 mm×0.5 mm, and the cell size is 0.5 μm. **Figure 8** illustrates the schematic diagram for the locations of the calculation domains A, B, and C. To clearly show the complete competition process between the columnar and equiaxed dendrites within the micro-scale calculation domains along the trailing pool boundary, the simulation for the competitive dendrite growth

is divided into two stages. Firstly, the columnar dendrites begin to grow form the bottom of the calculation domain. Owing to the small size of the calculation domain, the maximum temperature gradient direction does not change obviously within the calculation domain. In addition, according to the previous reference,[32] the orientations of the columnar dendrites do not exert the important influence on the CET result. As a result, to simplify the model, the preferential orientation of the columnar dendrite is uniform and normal to the trailing pool boundary in the present calculation. When the columnar dendrites come to the steady growth stage, the heterogeneous nucleation has been added in the model, and the competitive growth between columnar and equiaxed dendrites occurs. This method can illustrate the complete process of the competitive dendrite growth under various solidifica-

tion conditions along the trailing pool boundary and will not change the completion result of dendrites.

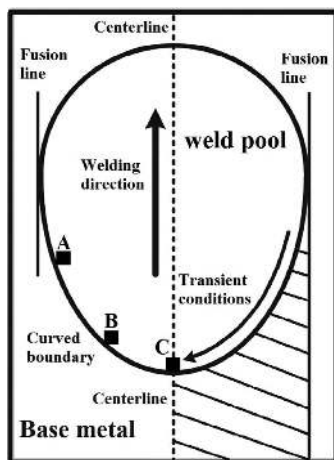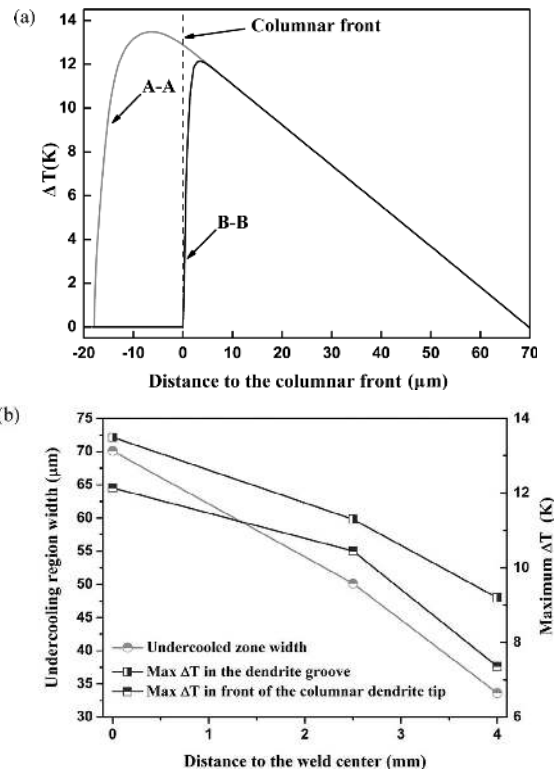**Figure 9** shows the columnar dendrite morphology in

Fig. 11. (a) The undercooling along the lines A-A and B-B in the calculation C. The *x* axis is the distance to the columnar front. (b) The undercooled zone width and the maximum undercooling in different calculation domains. The *x* axis is the distance to the weld center.

Fig. 8. The schematic diagram for the calculation domains of the competitive dendrite growth.
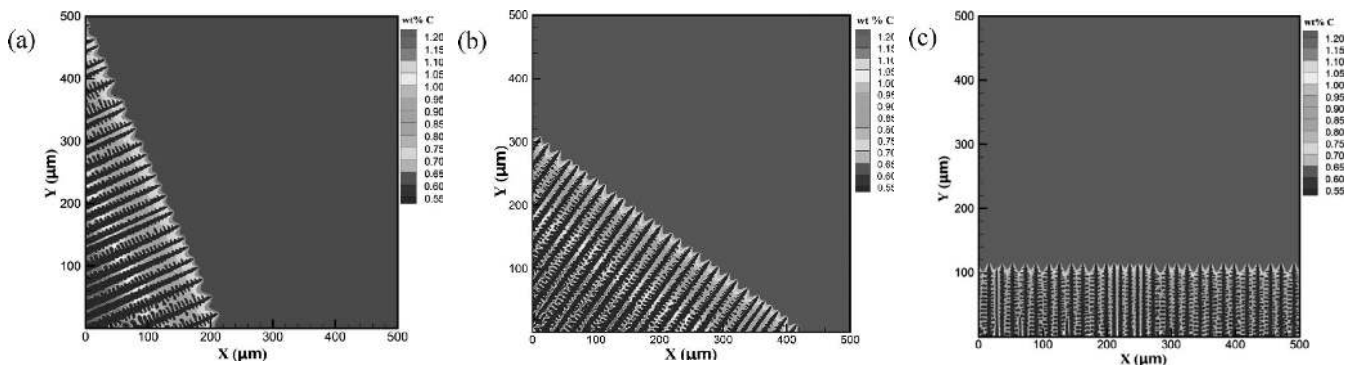

Fig. 9. The columnar dendrite morphology in the (a) calculation domain A, (b) calculation domain B, and (c) calculation domain C. The size of the calculation domain is 0.5 mm × 0.5 mm, and the cell size is 0.5 μm.
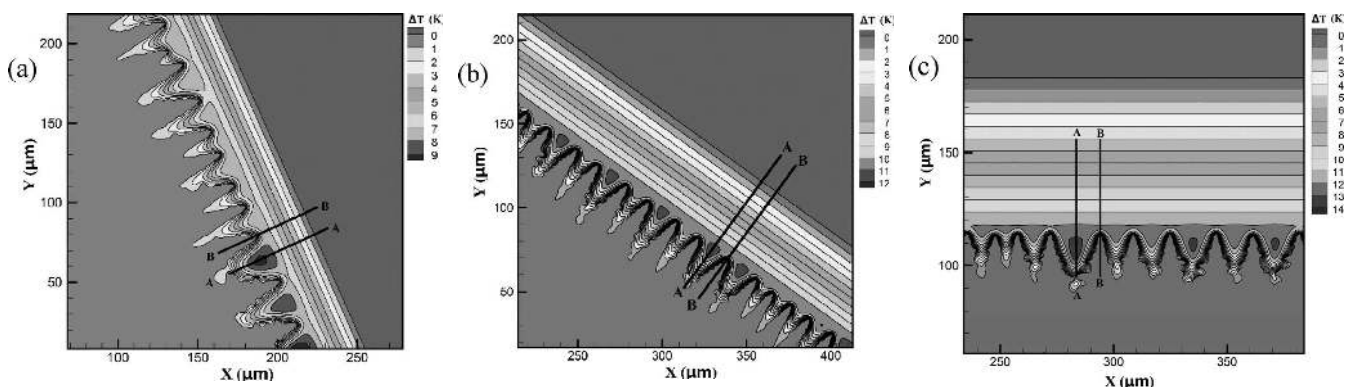

Fig. 10. The distribution of the undercooling in the (a) calculation domain A, (b) calculation domain B, and (c) calculation domain C.

the different calculation domains. The preferential orientation of the columnar dendrite is normal to the trailing pool boundary. It can be observed that the dendrite arm spacing decreases from the domain A to C. It is because that the cooling rate during solidification dominates the dendrite arm spacing and increases continuously from the fusion line to the weld center. The undercooled melt is the necessary condition for the nuclei to form and grow up. In the weld pool, the heat flow direction is always opposite to the solidification direction, and the temperature gradient in front

of the trailing pool boundary is always positive. Therefore, the undercooled zone only distributes near the trailing pool boundary. The undercooling ΔT can be calculated as follows:

$$\Delta T = [T_L + m_l(C_L - C_0)] - T^* \quad \text{...............} (15)$$

According to the Eq. (15), the liquid metal is undercooled if the undercooling ΔT is positive. **Figure 10** illustrates the distribution of the undercooling in different calculation domains. It can be seen that the area of the greatest
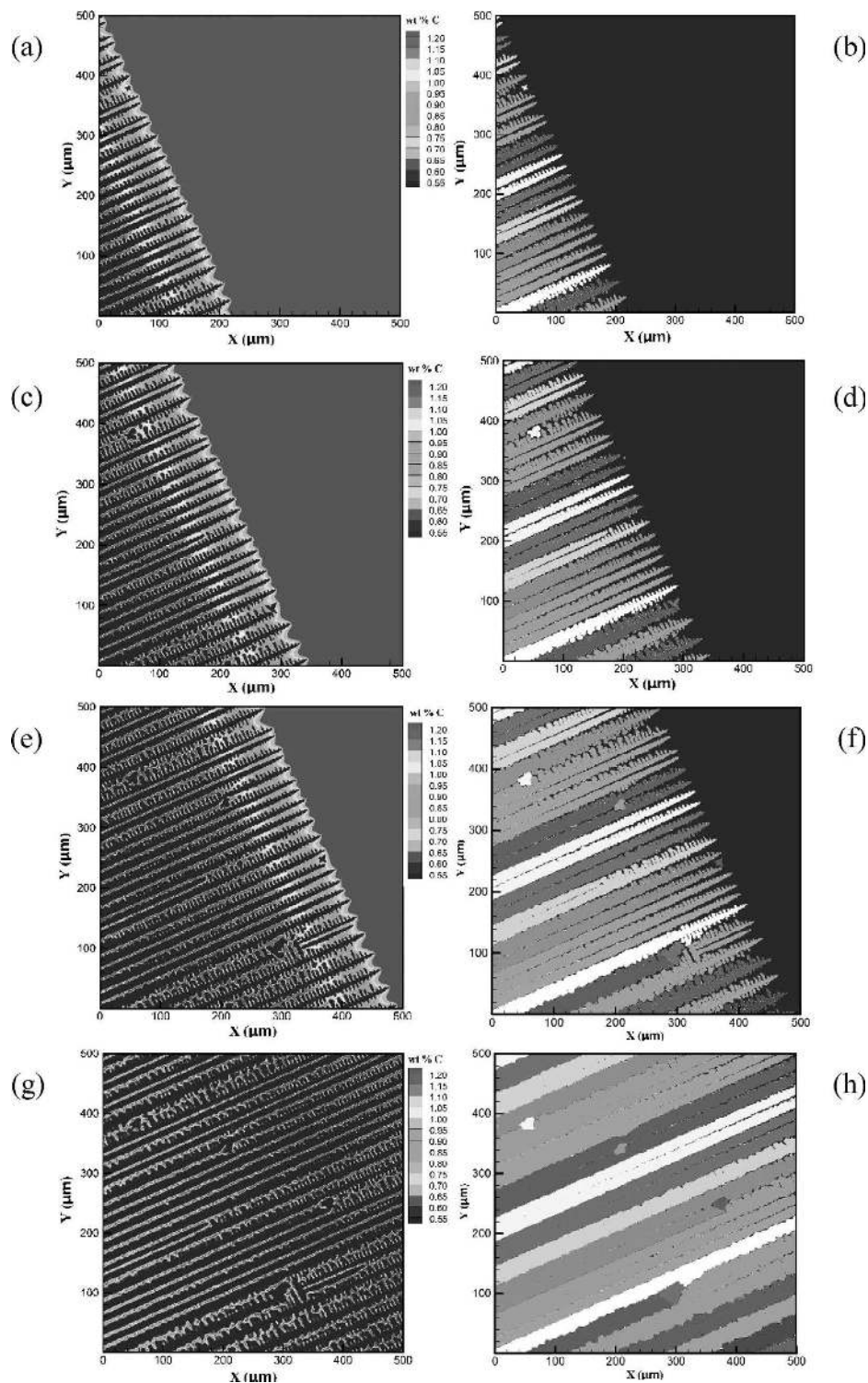

Fig. 12. The morphological evolution of solidification structures during the competitive dendrite growth in the calculation domain A. (a, c, e and g) show the evolution of the concentration field. (b, d, f and h) show the dendrite morphology evolution.

undercooling is clearly shown to be the columnar dendrite groove region rather than the region in front of the columnar tips. To accurately analyze the undercooling, the lines A-A and B-B as shown in Fig. 10 are selected to represent the columnar dendrite groove and the dendrite tip, respectively. **Figure 11**(a) shows the undercooling along the lines A-A and B-B in the calculation domain C. It can be observed that the undercooling increases rapidly to the maximum value and then decreases to 0 K again from the S/L interface to the liquid. The width of the undercooled zone in front

of the columnar tip is 70 μm. Figure 11(b) illustrates the undercooled zone width and the maximum undercooling in different calculation domains. It can be seen that from the calculation domain A to C, the undercooled zone width increases from 33.65 to 70 μm, the maximum undercooling in the dendrite grooves increases from 9.5 to 13.5 K.

Figure 12 shows the morphological evolution for the competitive dendrite growth in the calculation domain A. Near the fusion line, both the undercooled zone width and the maximum undercooling are small. The columnar den-
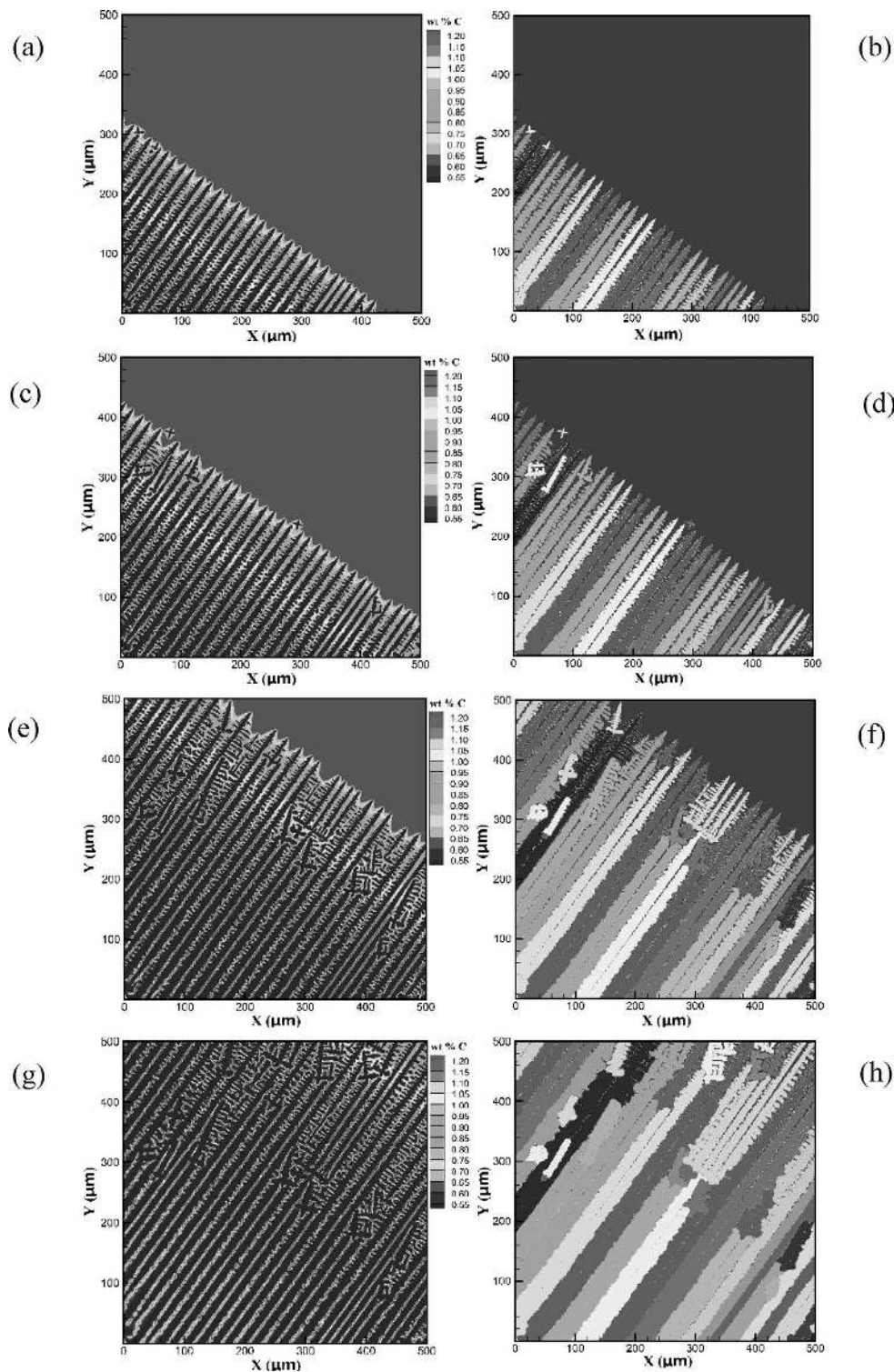

Fig. 13. The morphological evolution of solidification structures during the competitive dendrite growth in the calculation domain B. (a, c, e and g) show the evolution of the concentration field. (b, d, f and h) show the dendrite morphology evolution.

drite grooves have the maximum undercooling and hence are the favored locations for the heterogeneous nucleation. However, the equiaxed dendrite formed in the columnar dendrite groove is less competitive than the existing columnar dendrites around it in most cases. As a result, the interdendritic equiaxed grains appear as small "islands" in the final columnar region.[32] With the decrease of the distance to the weld center, both the undercooled zone width and the maximum undercooling increase. Therefore, it can be seen in **Fig. 13** that the number of the equiaxed dendrite increases correspondingly. Besides in the columnar dendrite grooves,

the equiaxed dendrites also form in front of the columnar dendrite tips. However, since the distance to the columnar dendrite tips is quite small, it is difficult for these equiaxed dendrites to grow up before the arriving of the columnar dendrites. Only a few favorably oriented equiaxed dendrites can grow up and block the columnar dendrites. Owing to the limited number of the surviving equiaxed grains, these grains has been elongated in the final solidification structure. **Figure 14** shows the simulated result in the calculation domain C. It can be observed that the number of the equiaxed dendrites increases rapidly. Since the undercooled
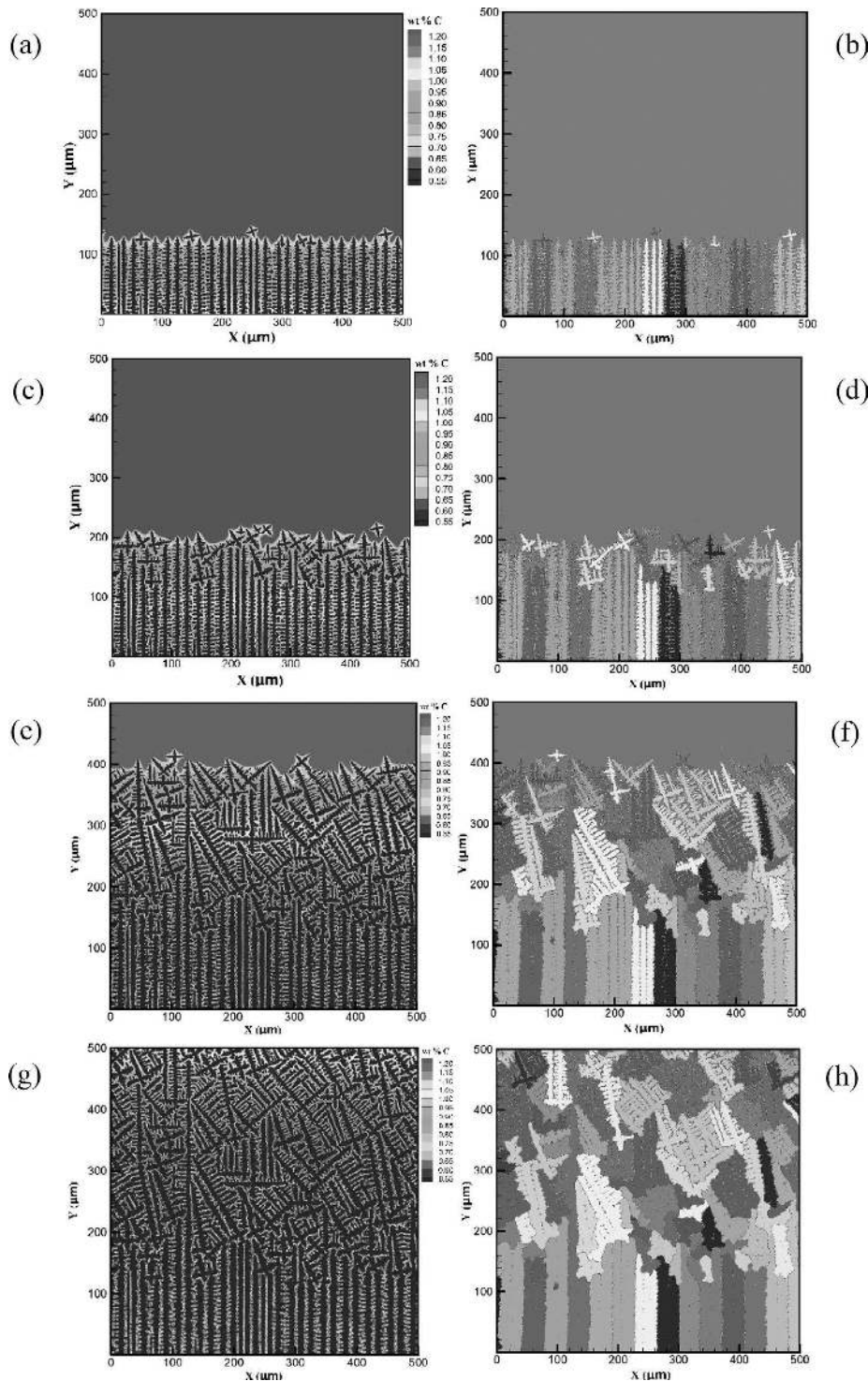

Fig. 14. The morphological evolution of solidification structures during the competitive dendrite growth in the calculation domain C. (a, c, e and g) show the evolution of the concentration field. (b, d, f and h) show the dendrite morphology evolution.
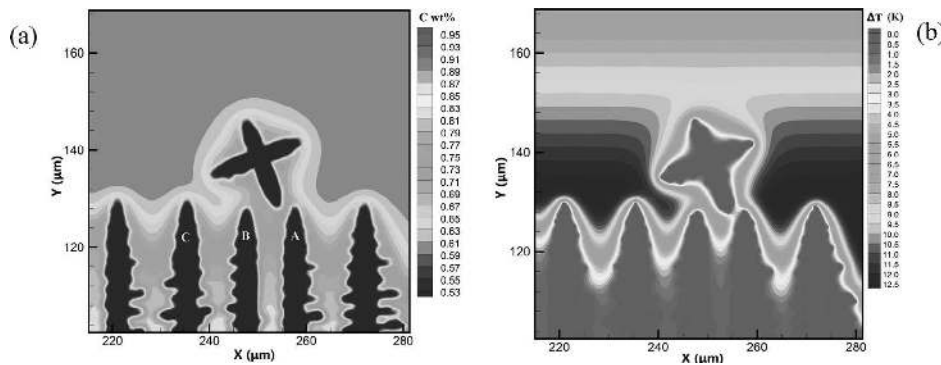
Fig. 15. The enlarged view of (a) the concentration field and (b) the undercooling distribution near the columnar front during the CET process.

zone width in the weld center is relatively large, more equiaxed dendrites are far away from the columnar dendrite tips. There is enough space for these equiaxed dendrites to grow up and occupy the growth path of the columnar dendrites. As a result, the columnar dendrites will be fully blocked and the CET occurs. The solute interactions has an important influence on the competitive dendrite growth. **Figure 15**(a) shows the enlarged view of concentration field near the columnar front during the CET process. It can be observed that the solute rejected by the growing equiaxed dendrite diffuses to the liquid. The competitive growth between the equiaxed and columnar dendrites occurs after the overlapping of the concentration field. The growth velocity of the columnar dendrites A, B and C which near the equiaxed dendrite decrease obviously before the contact of the dendrites. The accumulated solute near the equiaxed dendrite also affects the undercooling distribution. It can be found from the Fig. 15(b) that the undercooling around the equiaxed dendrite becomes lower. As a result, it is difficult to nucleate near the existing equiaxed dendrite. The results shown in sections 3.2 and 3.3 indicate that the change of the solidification conditions leads to the increase of both the undercooled zone width and the maximum undercooling from the fusion line to the weld center. The equiaxed dendrites are more competitive during the competition.

4. Conclusions

With the decrease of the distance to the weld center, the temperature gradient decreases and the solidification rate increases. Both the undercooled zone width and the maximum undercooling increase continuously owing to the change of the solidification conditions. In this case, more equiaxed dendrites form in the undercooled melt, and the distance between the equiaxed dendrites and the columnar front also becomes lager. There is more space for the equiaxed dendrites to grow up and block the columnar dendrites. As a result, the equiaxed dendrites become more competitive during the competitive growth, and the CET tendency increases form the fusion line to the weld center.

Acknowledgement

REFERENCES

1) T. DebRoy and S. A. David: *Rev. Mod. Phys.*, **67** (1995), 85.
2) S. A. David and J. M. Vitek: *Int. Mater. Rev.*, **34** (1989), 213.
3) S. Kou: Welding Metallurgy, John Wiley & Sons, Inc., Hoboken, NJ, (2002), 186.
4) V. Pavlyk and U. Dilthey: *Model. Simul. Mater. Sci. Eng.*, **12** (2004), S33.
5) Y. Wei, X. Zhan, Z. Dong and L. Yu: *Sci. Technol. Weld. Join*, **12** (2007), 138.
6) X. Zhan, Z. Dong, Y. Wei and R. Ma: *J. Cryst. Growth*, **311** (2009), 4778.
7) X. Zhan, Y. Wei and Z. Dong: *J. Mater. Process. Technol.*, **208** (2008), 1.
8) R. Ma, Z. Dong, Y. Wei, X. Zhan and Y. Wang: *Cryst. Res. Technol.*, **44** (2009), 1197.
9) Z. Dong, S. Wang, R. Ma, Y. Wei, K. Song and G. Zhai: *J. Mater. Sci. Technol.*, **27** (2011), 183.
10) H. Yin and S. D. Felicelli: *Acta Mater.*, **58** (2010), 1455.
11) S. Chen, G. Guillemot and C. A. Gandin: *ISIJ Int.*, **54** (2014), 401.
12) C. Bordreuil and A. Niel: *Comp. Mater. Sci.*, **82** (2014), 442.
13) W. Tan, S. Wen, N. Bailey and Y. C. Shin: *Metall. Mater. Trans. B*, **42** (2011), 1306.
14) W. Tan, N. S. Bailey and Y. C. Shin: *J. Manuf. Sci. Eng.*, **134** (2012), 041010.
15) W. Tan and Y. C. Shin: *Comput. Mater. Sci.*, **98** (2015), 446.
16) A. Farzadi, M. Do-Quang, S. Serajzadeh, A. Kokabi and G. Amberg: *Model. Simul. Mater. Sci. Eng.*, **16** (2008), 065005.
17) V. Fallah, M. Amoorezaei, N. Provatas, S. Corbin and A. Khajepour: *Acta Mater.*, **60** (2012), 1633.
18) W. J. Zheng, Z. B. Dong, Y. H. Wei, K. J. Song, J. L. Guo and Y. Wang: *Comput. Mater. Sci.*, **82** (2014), 525.
19) W. Zheng, Z. Dong, Y. Wei and K. Song: *J. Cryst. Growth*, **402** (2014), 203.
20) W. C. Dong, S. P. Lu, D. Z. Li and Y. Y. Li: *Int. J. Heat Mass Transf.*, **54** (2011), 1420.
21) T. Ganaha, B. Pearce and H. Kerr: *Metall. Trans. A*, **11** (1980), 1351.
22) B. Pearce and H. Kerr: *Metall. Mater. Trans. B*, **12** (1981), 479.
23) S. Kou and Y. Le: *Metall. Mater. Trans. A*, **13** (1982), 1141.
24) S. Kou and Y. Le: *Metall. Mater. Trans. A*, **16** (1985), 1887.
25) C. S. Wu: Weld Thermal Process and Weld Pool Shape, China Machine Press, Beijing, (2007), 123.
26) L. Beltran-Sanchez and D. M. Stefanescu: *Metall. Mater. Trans. A*, **35** (2004), 2471.
27) S. Luo and M. Y. Zhu: *Comput. Mater. Sci.*, **71** (2013), 10.
28) M. F. Zhu and D. M. Stefanescu: *Acta Mater.*, **55** (2007), 1741.
29) M. Nakagawa, Y. Natsume and K. Ohsasa: *ISIJ Int.*, **46** (2006), 909.
30) M. Rappaz and C. A. Gandin: *Acta Metall. Mater.*, **41** (1993), 345.
31) C. A. Gandin and M. Rappaz: *Acta Metall. Mater.*, **42** (1994), 2233.
32) H. B. Dong and P. D. Lee: *Acta Mater.*, **53** (2005), 659.
33) J. Lipton, M. Glicksman and W. Kurz: *Mater. Sci. Eng.*, **65** (1984), 57.
34) L. Beltran-Sanchez and D. M. Stefanescu: *Metall. Mater. Trans. A*, **34** (2003), 367.
35) J. J. Blecher, T. A. Palmer and T. DebRoy: *Metall. Mater. Trans. A*, **45** (2013), 2142.
36) W. Kurz and D. J. Fisher: Fundamentals of Solidification, Trans Tech Publications, Switzerland, (1998), 88.